MethodsX 13 (2024) 102799

Contents lists available at ScienceDirect

MethodsX

journal homepage: www.elsevier.com/locate/methodsx

# Integrated methodology for gas content assessment and prediction in shallow muddy lake sediments: acoustic mapping and correlation analysis☆

E. Uzhansky[a,b,*], R. Katsman[a], A. Lunkov[c], B. Katsnelson[a]

[a] Dr. Moses Strauss Department of Marine Geosciences, Leon H. Charney School of Marine Sciences, University of Haifa, Haifa, Israel
[b] Dynamics Lab, Mechanical Engineering, Technion – Israel Institute of Technology, Haifa, Israel
[c] Prokhorov General Physics Institute of the Russian Academy of Sciences, Russia

A R T I C L E  I N F O

*Method name:*
Integrated Methodology for Gas Content Assessment: Geoacoustic Inversion and Correlation Analysis

*Keywords:*
Methane bubbles
Gassy sediment
Acoustic application
Geoacoustic inversion
Regression analysis

A B S T R A C T

This paper provides a step-by-step description of integrated methodology for quantification and prediction of gas (methane, $CH_4$) content dynamics in shallow aquatic sediments under changing spatial and temporal conditions. Presence of gas bubbles even in small concentrations significantly affects sediment compressibility, which in turn decreases sound speed in sediment. Our integrated methodology consists of two basic steps. In the first step, free gas content is evaluated by acoustic applications based on the sound speed inferred from the reflection coefficient from gassy bottom. The experimental bottom reflections are registered and compared to the simulated ones, using a geoacoustic inversion technique. The best match between the model and the experiment provides sediment sound speed estimate, which is converted into free gas content using a basic relation. In the second step, a multivariate linear regression is fitted for gas content and closed form expression of gas content dependence on the following predictors, which change spatially and temporally over the aquatic ecosystem, is obtained: 1) water depth, 2) short-leaving $CH_4$ production rate peaks fueled by punctuated organic matter deposition; and 3) $CH_4$ bubble dissolution rates.

- Gas content and sound speed in the sediment are estimated via the geoacoustic inversion technique by matching the experimentally recorded and simulated bottom reflections
- Only single source and receiver are required for the acoustic methodology
- A multivariate linear regression is fitted for gas content to indicate its dependence on various predictors that change spatially and temporally over the lake

## Specifications table

| | |
|---|---|
| Subject area | Earth and Planetary Sciences |
| More specific subject area | Acoustical Oceanography |
| Name of your method | Integrated Methodology for Gas Content Assessment: Geoacoustic Inversion and Correlation Analysis |
| Name and reference of original method | Acoustic remote sound speed estimation in the gassy sediment |
| Resource availability | Data availability: Raw data used in this paper can be found in supplementary material |

☆ **For a published article:** Katsman R., Uzhansky E., Lunkov A., Katsnelson B., Methane Gas Dynamics in Sediments of Lake Kinneret, Israel, and Their Controls: Insights from a Multiannual Acoustic Investigation and Correlation Analysis, STOTEN, (2024), https://doi.org/10.1016/j.scitotenv.2024.170480.
DOI of original article: 10.1016/j.scitotenv.2024.170480

* Corresponding author.
*E-mail address:* ernstu@technion.ac.il (E. Uzhansky).

https://doi.org/10.1016/j.mex.2024.102799
Received 12 February 2024; Accepted 10 June 2024
Available online 11 June 2024

## Method details

Gaseous methane ($CH_4$) frequently occurs in organic-rich aquatic and terrestrial sediments [1]. It represents the most prevalent hydrocarbon and ranks among the primary greenhouse gases in the atmosphere. Various methodologies are available to estimate the gas content within shallow near-surface sediments. Methods for assessing gas content within sediments are traditionally divided into direct and remote ones.

Among direct methods, the X-ray computer tomography (CT) scanning of sediment cores obtained under in situ pressure and temperature allow for identifying and quantifying gas bubbles within the core [2] at high (0.04 $mm^3$ voxel size) spatial resolution [3]. Considering large spatial and temporal variability of gas bubble concentration in the sediment [4], measurements of free gas content with pressurized gravity corers or freeze corers are time- and labor-consuming, expensive and, therefore, practically unfeasible for studying large areas. In addition, corers can damage the sediment during the sampling process, which may affect the free gas content and its quantitative estimates in the cores [3]. As another example of direct methods, in situ acoustic methodologies entail the utilization of either manually deployed buried acoustic systems [5] or specially engineered underwater mechanical systems capable of penetrating sediment layers via gravitational forces [6,7]. While such methodologies contribute to maintaining in situ conditions, they too may inadvertently disturb sediments during device installation.

Remote acoustic techniques for gauging gas content in sediments capitalize on the marked alteration in compressibility resulting from even minor gas fractions, leading to a notable reduction in sediment sound speed [8]. This alteration also influences other geoacoustic properties of the sediment. Some of those methods include measurement and analysis of the bottom reflection coefficient and studying the amplitude-frequency characteristics of the sound field as a function of sound speed in the sediment [9]. Also, studies of the acoustic properties of gassy sediments have been conducted via analysis of the resonance and nonlinear properties of gas bubbles in water/sediment, and their aggregations [10]. Seismo-acoustic methods and high-frequency echo sounders have been implemented to map the existence of gassy sediment (without information about gas content) and its spatial distribution [11]. In [12], Tõth and coauthors applied migration velocity analysis of pre-stack time-migrated data and quantified free gas content in shallow sediments in the Baltic Sea. However, many of conventional seismic methods are not applicable to gassy sediments. For instance, methods based on the slope of the head wave arrival [13,14] or on the position of caustics due to ray bending in the sub-bottom [15], will not work with gas-saturated sediments. This is because the sound speed in such sediments is lower than in water, and all rays, according to Snell's law, are directed downwards and do not experience total internal reflection.

In this paper, we present a multimethodological approach allowing remote estimation and correlation of gas content dynamics in aquatic muds with various local predictors. Gas content is evaluated by remote acoustic applications, presented in Section 1 below. Method assumptions, limitations, instrumentation, followed by detailed experimental validation are presented in Sections 1.1 – 1.6. Step-by-operation description is presented in Section 1.7. Correlation analysis methodology is presented in Section 2.

## Acoustic methodology of gas content evaluation in aquatic muds

### *Acoustic model assumptions*

The incorporation of gas bubbles into marine sediment fundamentally alters its acoustical properties, with a pronounced impact on the effective compressibility of the sediment. This, in turn, affects the compressional sound speed and to lesser extend density of the sediment, which leads to changes in acoustic impedance of the sediment and the corresponding reflection coefficient at the water-sediment interface [16,17]. Thus, acoustic properties of gas-bearing sediments can be systematically investigated using acoustical techniques. Given that the sound frequencies and the corresponding wavelengths of sound waves employed in the method are significantly greater than the dimensions of the bubbles, the gaseous sediment layer can be modeled as a homogeneous "liquid" half-space. In this model, it is assumed that sediment supports only compressional waves, whereas shear waves are negligible [17].

### *Model of sound speed and reflection from gassy bottom*

In our experiment, sound signal is radiated by a sound source and recorded by a hydrophone deployed at depths of $z_s$ and $z_r$, respectively, which are separated by distance $r_{rs}$. The thickness of the water layer is H (Fig. 1). The densities of water and bottom sediments are denoted by $\rho_w$ and $\rho$, respectively, the sound speed by $c_w$ and c, and the angle of incidence by $\theta$.

At a low frequency (wavelength of the sound wave is bigger than gas bubble size), effective sound speed in gassy sediment can be described in the framework of three-component (water, rigid particles, and gas) sediment model [18]:

$$c = \frac{c_w}{n_w}\left[\left(1+\frac{n_s\rho_s}{n_w\rho_w}+\frac{n_g\rho_g}{n_w\rho_w}\right)\left(1+\frac{n_s c_w^2\rho_w}{n_w c_s^2\rho_s}+\frac{n_g c_w^2\rho_w}{n_w c_g^2\rho_g}\right)\right]^{-\frac{1}{2}} \quad (1)$$

Here $c_w$, $n_w$, $\rho_w$, $c_s$, $n_s$, $\rho_s$, $c_g$, $n_g$, $\rho_g$ are the sound speeds, fractions and densities of water, of rigid particles, and of gas in bottom sediments, respectively. Fig. 2b illustrates function $c(n_g)$ at three levels of the water fraction, $n_w$, evaluated from Eq. (1). Geoacoustic parameters of the medium components are presented in Table 1. Even small amounts of gas content in sediments substantially affect the speed of sound in the sediment (Fig. 2a). Sound speed in the sediment becomes 10 times less than that in water at $n_g < 1\%$.

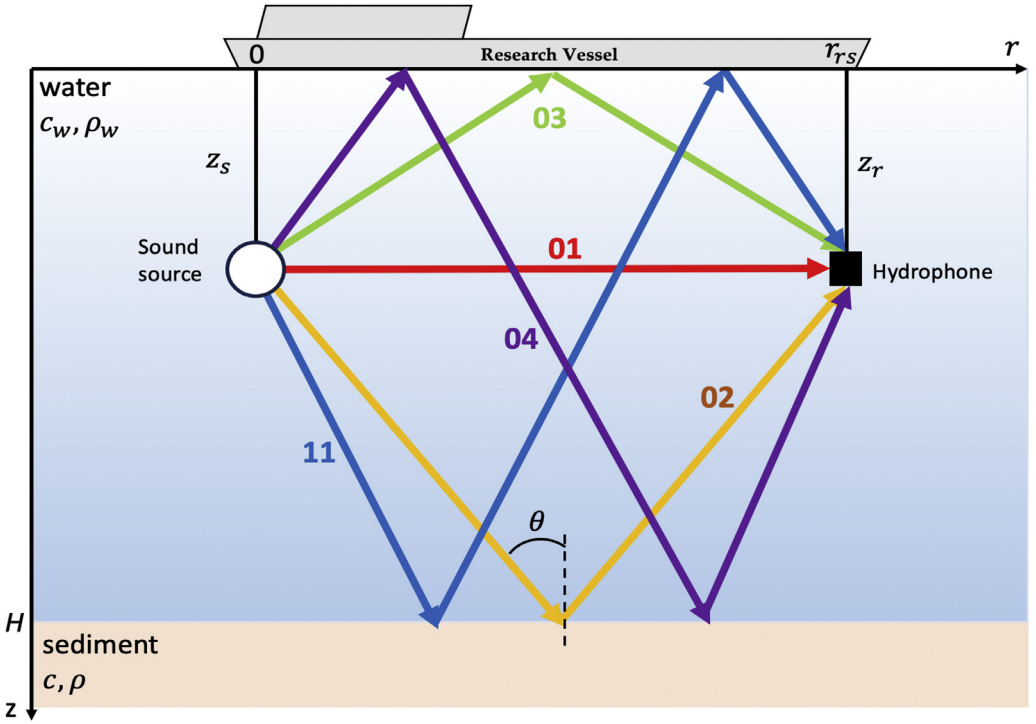


**Fig. 1.** Sketch of the acoustic experiment. Sound reflection from the boundaries is illustrated with arrows, where numbers indicate indices [l, j] corresponding to each arrival. θ is the angle of incidence of the ray.

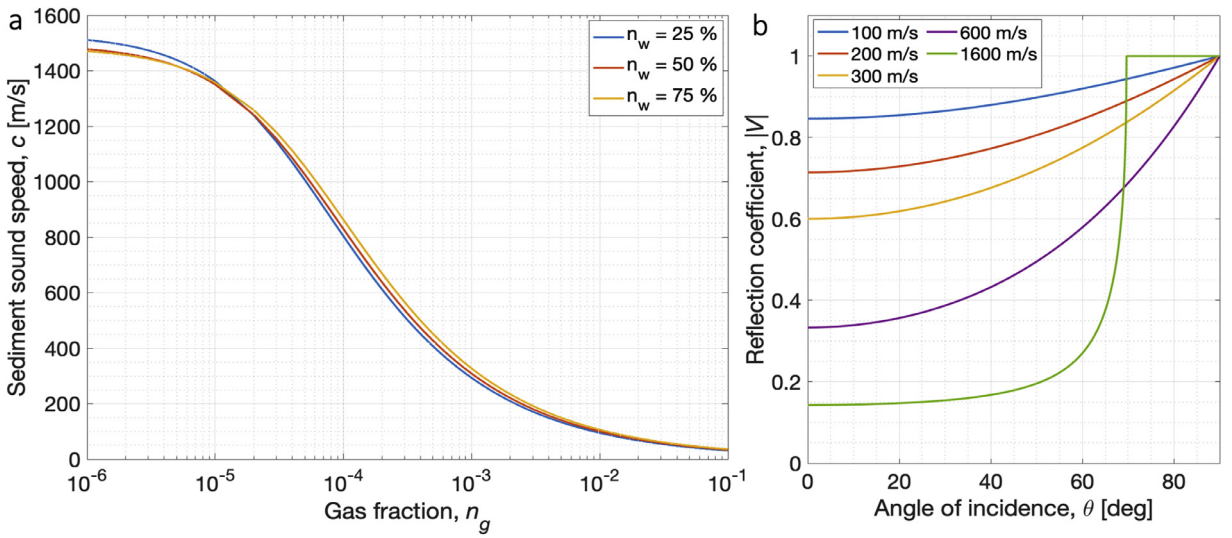


**Fig. 2.** a) Sound speed in gassy sediment, c, as a function of gas fraction, $n_g$, at different values of water saturation, $n_w$; b) absolute value of the reflection coefficient, |V|, as a function of angle of incidence, θ, at different values of sound speed in sediments, c;.

**Table 1**
Acoustic and physical parameters of sediment components.

| Medium | Rigid particles | Water | Methane |
|---|---|---|---|
| Sound speed | $c_s$ = 1600 m/s | $c_w$ = 1500 m/s | $c_g$ = 430 m/s |
| Density | $\rho_s$ = 1.6 g/cm$^3$ | $\rho_w$ = 1 g/cm$^3$ | $\rho_g = 7 \cdot 10^{-4}$ g/cm$^3$ |

**Table 2**
Parameters for acoustic simulation using ray theory.

| Parameters | Values |
|---|---|
| Water column: $c_w$, $\rho_w$ | 1500 m/s, 1000 kg/m$^3$ |
| Sediment: $\boldsymbol{c}$, $\boldsymbol{\rho}$ | $300\boldsymbol{m/s}$, $1450\boldsymbol{kg/m}^3$ |
| Water depth and source-receiver range, $\boldsymbol{H}$, $\boldsymbol{r_{rs}}$ | 30 m, 1 m |
| Source and receiver depth, $\boldsymbol{z_s} = \boldsymbol{z_r}$ | 10 m, 20 m |
| Signal type | Pulse |
| Signal duration, $\boldsymbol{T}$ | 0.1 ms |

The Rayleigh reflection coefficient at water-sediment interface is given by [17]:

$$V = \frac{\frac{\rho}{\rho_w}\cos\theta - \sqrt{\left(\frac{c_w}{c}\right)^2 - \sin^2\theta}}{\frac{\rho}{\rho_w}\cos\theta + \sqrt{\left(\frac{c_w}{c}\right)^2 - \sin^2\theta}} \tag{2}$$

Fig. 2b shows absolute value of the reflection coefficient, $|V(\theta)|$, for various c. When $c \ll c_w$, the reflection coefficient is very high, even at normal incidence (i.e., $\theta = 0°$). For instance, at $c = 100$ m/s, the absolute value of the reflection coefficient is $|V| \sim 0.85$ (real value of the reflection coefficient is negative), and its phase is $\approx \pi$. One can see an absence of the total internal reflection in case of even small gas fractions in the sediment. These two phenomena of gassy sediments, low sound speed and high reflection coefficient, present the basis of our methodology for gas content assessment.

*Shallow water waveguide with gassy bottom*

For simulations, we use ray propagation theory described in Brekhovskikh & Lysanov [17]. A waveguide with a constant depth H (Fig. 1) is used. The point sound source is located at the point $r = 0,\ z = z_s$ and radiates signal $s(t)$. For such a case, the acoustic signal $P(t)$ received by a single hydrophone located at $r = r_{rs},\ z = z_r$, is composed of multiple signals reflected from the bottom and water surface. It can thus be presented as a sum of rays:

$$P(t) = \sum_{l=0}^{\infty}\left[\left(-V_{l1}\right)^l \frac{s\left(t - \frac{R_{l1}}{c_w}\right)}{R_{l1}} - \left(-V_{l2}\right)^{l+1}\frac{s\left(t - \frac{R_{l2}}{c_w}\right)}{R_{l2}} - \left(-V_{l3}\right)^l \frac{s\left(t - \frac{R_{l3}}{c_w}\right)}{R_{l3}} + \left(-V_{l4}\right)^{l+1}\frac{s\left(t - \frac{R_{l4}}{c_w}\right)}{R_{l4}}\right]. \tag{3}$$

Here, $R_{lj} = \sqrt{r_{rs}^2 + z_{lj}^2}$, $j = 1, 2, 3, 4; l = 0, 1, 2, \ldots$ (j and l are indices defining a ray number in a quadrupole of rays and a quadrupole number, respectively), $r_{rs}$ is the horizontal range between the source and receiver (Fig. 1).

The equivalent source depths, $z_{lj}$, for each ray is expressed as follows:

$$z_{l1} = 2lH + z_s - z_r,\ z_{l2} = 2(l+1)H - z_s - z_r, \tag{4a}$$

$$z_{l3} = 2lH + z_s + z_r,\ z_{l4} = 2(l+1)H - z_s + z_r, \tag{4b}$$

where $V_{lj}$ is the reflection coefficient at the water-sediment interface that can be calculated using Eq. (2) with the angle of incidence, $\theta$, replaced by $\theta_{lj} = \arcsin(\frac{r_{rs}}{R_{lj}})$.

Fig. 3 shows simulated pulse signal envelope at a hydrophone for parameters presented in Table 2. Each arrival corresponds to one or two rays. The reflection coefficient, $|V| \sim 0.6$ and is independent of frequency. Such a highly reflective bottom leads to the appearance of a sequence of signals repeatedly reflected from the bottom and water surface.

An important thing when processing experimental data, is the dependence of the ray arrival order on the relationship between the depth of the reservoir and the depth of the source-receiver. For a 30-m deep reservoir, if the source-receiver system is deployed at a small depth, $\boldsymbol{z_s} = \boldsymbol{z_r} = 10$m (Fig. 3a), the direct signal arrives first, followed by the surface reflected signal and bottom reflected one. In a case when the source-receiver system is deployed closer to the bottom, $\boldsymbol{z_s} = \boldsymbol{z_r} = 20$m (Fig. 3b), the bottom reflection arrives before the surface reflection.

*Geoacoustic inversion methodology*

Our methodology includes a geoacoustic inversion procedure based on analysis of sound signals recorded by receivers in the water layer (Fig. 1), which contain information about the medium through which they have traveled (proposed in [19], extended in [4,20–22].) The essence of the method is that experimentally measured sound reflection coefficient from the sediment is juxtaposed with the numerically modeled one (Sectioin 1.3), to estimate effective sound speed in the sediment, which is subsequently converted into gas content via Eq. (1).

When estimating the reflection coefficient, one should process as many ray arrivals as possible, including multiple reflections (10 separate peaks are marked in Fig. 3 with black dashed lines; note that some arrivals overlap, i.e., at $t = 0.08$ and 0.12 s). To find the

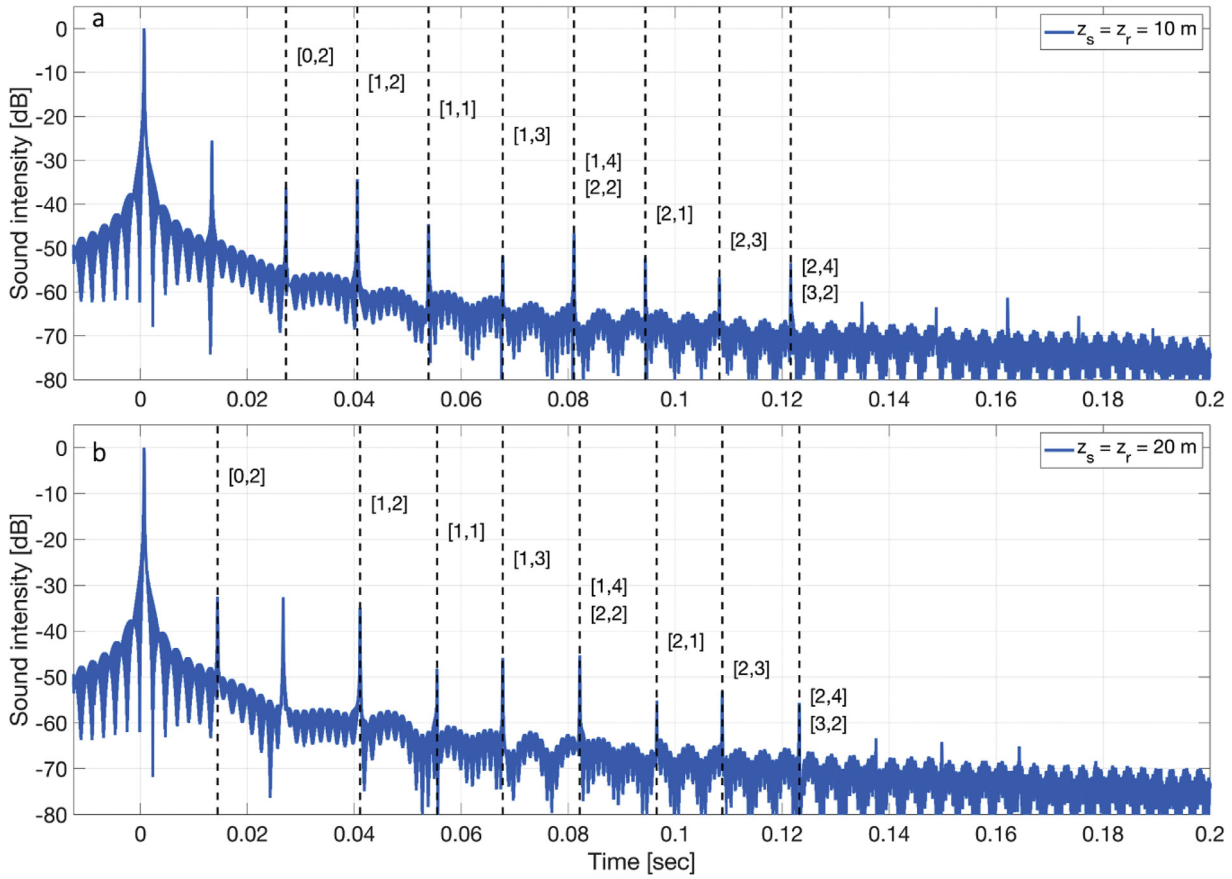


**Fig. 3.** Example illustrating an envelope of the simulated pulse signal at a hydrophone (Fig. 1) for the sediment sound speed of 300 m/s. A series of bottom reflections and their multiples are shown by black dashed lines. Indices $[l, j]$ corresponding to each arrival, are displayed near each line. $\boldsymbol{H}$ = 30m, $\boldsymbol{r_{rs}}$ = 1m, a) $z_s = z_r = 10$ m, b) $z_s = z_r = 20$ m.

best fit between the experimental arrivals and the simulated ones, the matched-field processing (MFP) is applied. The envelopes of the experimental and simulated signals are compared on a logarithmic scale:

$$\boldsymbol{F}(c) = \left( \frac{1}{\boldsymbol{N}} \sum_{i=1}^{\boldsymbol{N}} \left| 20 \log \boldsymbol{B}_{\boldsymbol{mod}}(t_i; c) - 20 \log \boldsymbol{B}_{\boldsymbol{exp}}(t_i) \right| \right)^{-1} \tag{5}$$

where $\boldsymbol{B}_{\boldsymbol{mod}}$ and $\boldsymbol{B}_{\boldsymbol{exp}}$ are the envelopes of the simulated and experimental signals, respectively; $\boldsymbol{t_i}$ is the $\boldsymbol{i}$-th pulse arrival time. The total number of analyzed pulses ($\boldsymbol{N}$) depends on the number of the experimentally detected arrivals.

The effective sound speed, $\boldsymbol{c}$, corresponds to the maximum of $\boldsymbol{F}(\boldsymbol{c})$, which is obtained for each radiated chirp. Resulting $\boldsymbol{c}$ is obtained as a mean of all estimated sound speeds for all chirps radiated in the corresponding geographical point. The final estimate of $\boldsymbol{c}$ is described as $\boldsymbol{c_{best}} \pm \boldsymbol{M E_c}$, representing the 95% confidence interval. The margin of error, $\boldsymbol{M E_c}$, represents the standard error of the mean value of sound speed, multiplied by the calculated 95% values of Student's $\boldsymbol{t}$ inverse cumulative distribution function. Resulting estimates on the free gas content are performed using the relationship between sound speed and free gas content (Eq. (2), Fig. 2a). Due to the power law dependence, the free gas content error cannot be calculated as $\boldsymbol{\Theta_{gas}} \pm \boldsymbol{M E_\Theta}$, thus, it is presented as an interval corresponding to $\boldsymbol{\Theta_{gas}}(\boldsymbol{c_{best}} - \boldsymbol{M E_c})$ and $\boldsymbol{\Theta_{gas}}(\boldsymbol{c_{best}} + \boldsymbol{M E_c})$.

*Implementation: acoustic setup and measurements*

The implementation of the method requires a sound source (with a signal generator and an amplifier), a single hydrophone and a data acquisition card (DAQ). In our case, we used LL-9162T underwater sound speaker (by LUBELL, Fig. 4a) and BII-7017 hydrophone (by Benthowave, Fig. 4b) connected to a data acquisition card (DAC). Several alternative implementation configurations are suggested below. If one already has an external signal generator (in our case, we used dual channel arbitrary/function generator AFG3022C by Tektronix), one needs a separate DAQ to record the acoustic data. For instance, NI USB-6001 (by National Instruments, Fig. 4c) has seven analog input channels. Alternatively, to use more than 7 channels simultaneously (e.g., a vertical hydrophone array covering the whole reservoir depth), there are other DAQs available (e.g., NI USB-6211 and NI USB-6216). If one has neither a signal


**Fig. 4.** Experimental setup for acoustic data acquisition. a) Underwater sound speaker Lubell LL-9162T, b) omnidirectional widbeand hydrophone Benthowave BII-7017, c) analog-digital converter NI USB-6001, d) multi-instrument device Analog Discovery 3 with two analog input and two analog output channels connected via e) the BNC adaptor.

generator, nor a DAQ, a recently released multi-instrument device Analog Discovery 3 (by Digilent) can serve as a convenient option for simultaneous signal radiation and acquisition of the acoustic data (Fig. 4d). It has two analog inputs and two analog outputs with high sampling rates (Fig. 4e).

In our experiment (Fig. 1), the sound source and the receiver are placed at the depth of $z_s$ and $z_r$, respectively, and are separated horizontally by distance $r_{rs}$. To preserve a constant distance between the source and the receiver, one can tie the hydrophone and the source by a thin solid rod. The rod should made of material with density and sound speed close to that in water, so that the sound reflection from it will be weak.

Due to the proximity of arrival times of the direct and reflected signal (tens of milliseconds), arrivals may overlap and may become hardly separable. This can complicate the acoustic data processing and analysis and spoil the quality of the gas content estimates. The geometrical configuration (parameters $z_s$, $z_r$, $r_{rs}$, Fig. 1) is strongly dependent on the water depth $H$ and should be considered thoroughly before each measurement. Optimal source-receiver depths can be found in section Optimal source-receiver configuration in [22] along with description of its calculation.

Wavelengths of the sound waves should be significantly bigger than the gas bubble diameter. In our experiments, we used 1-s and 5-s long chirps in the frequency bands of either 300 – 2000 Hz or 300 – 3500 Hz. There are several important limitations on the signal frequencies that could be considered. First one is related to directionality of the sound source. In our case, Lubell LL-9162T is omnidirectional at frequencies < 3.5 kHz, but becomes strongly directive at higher frequencies. In our experiments, we limited the upper frequency to 3.5 kHz. If one wants to employ sound signals at higher frequencies, it is necessary to correct for the directionality pattern of the source, or to use another transducer, which is omnidirectional at high frequencies (one can check for spherical transducers). The correction can be performed by securing the speaker to a frame, to avoid its rotation under water. Second limitation is related to resonance (the Minnaert resonance) frequency of gas bubbles. Katsman et al. [23] demonstrated that sediment sound speed, sediment attenuation coefficient, and reflection coefficient at the water-sediment interface, show non-linear frequency dependence, which are controlled by the bubble size, cumulative gas content, and corresponding resonant frequency of the gas bubble. This limits the sharpness of the pulse, which width is inversely proportional to the frequency band of the chirp. At small water depths, this may make the arrivals hardly distinguishable one from another, whereas their interference can affect the amplitude of the reflection and bias the sound speed estimates.

*Method validation: acoustic data processing and analysis*

Processing, analysis and validation of the acoustic data acquired in the experiments carried out in May 2019 in Lake Kinneret, Israel, is presented below. The original file containing raw acoustic data (in Volts) can be found in Supplementary material section. The LUBELL LL-9162T sound source was deployed at the depth, $z_s$, of 11m (Fig. 1). A Benthowave BII-7017 hydrophone with a flat sensitivity response of −174.5 (±2) dB (re V/$\mu$Pa from 0.1 to 100 kHz) was deployed at the same depth 1 m away from the sound source. The water depth, $H$, was 17 m. A series of 1-s long linear frequency modulated pulses (chirps) in the frequency band of 300–3500 Hz were radiated with 5-s pauses (Fig. 5a-c). Twenty pulses were recorded in total at the same geographical point to ensure repeatability of the acoustic results. The sound transducer has a curved frequency response which deforms the shape of the radiated chirp (Fig. 5a). The sampling frequency was set to 20 kHz, and the geometric configuration of source-recorded was set following the calculations presented in [22]. Sound speed profile was calculated from CTD measurement. Due to the short propagation times and small angles of incidence, the water layer can be represented as homogeneous with a depth-averaged $c_w$ = 1485 m/s.

Fig. 5c shows an example of the recorded acoustic data. The recorded signals were cross-correlated with the radiated one (Fig. 5a) to obtain an impulse response function (Fig. 5d). Due to presence of gas bubbles the signal exhibits multiple reflections from the waveguide boundaries (Fig. 5e). In the experiment, the research vessel was not anchored and, despite calm weather and low surface currents, was drifting by about 100–200 m. This increased the uncertainty and made the results of estimates to represent an effective value for some area. The assessment of the bottom ensonification area can be found in [22]. In our case, this area for a stationary source is 18 m$^2$.

An example illustrating a comparison between the experimentally recorded data and three simulations ($c$ = 100 m/s, 500 m/s, 1000 m/s) is shown in Figs. 6a-c. Due to high number of seafloor reflections, $N$ was chosen to be 18. Fig. 6d shows the normalized cost functions $F(c)$ (see Eq. (5)) calculated for each radiated pulse (black curves correspond to 20 radiated signals) and their mean $\overline{F(c)}$

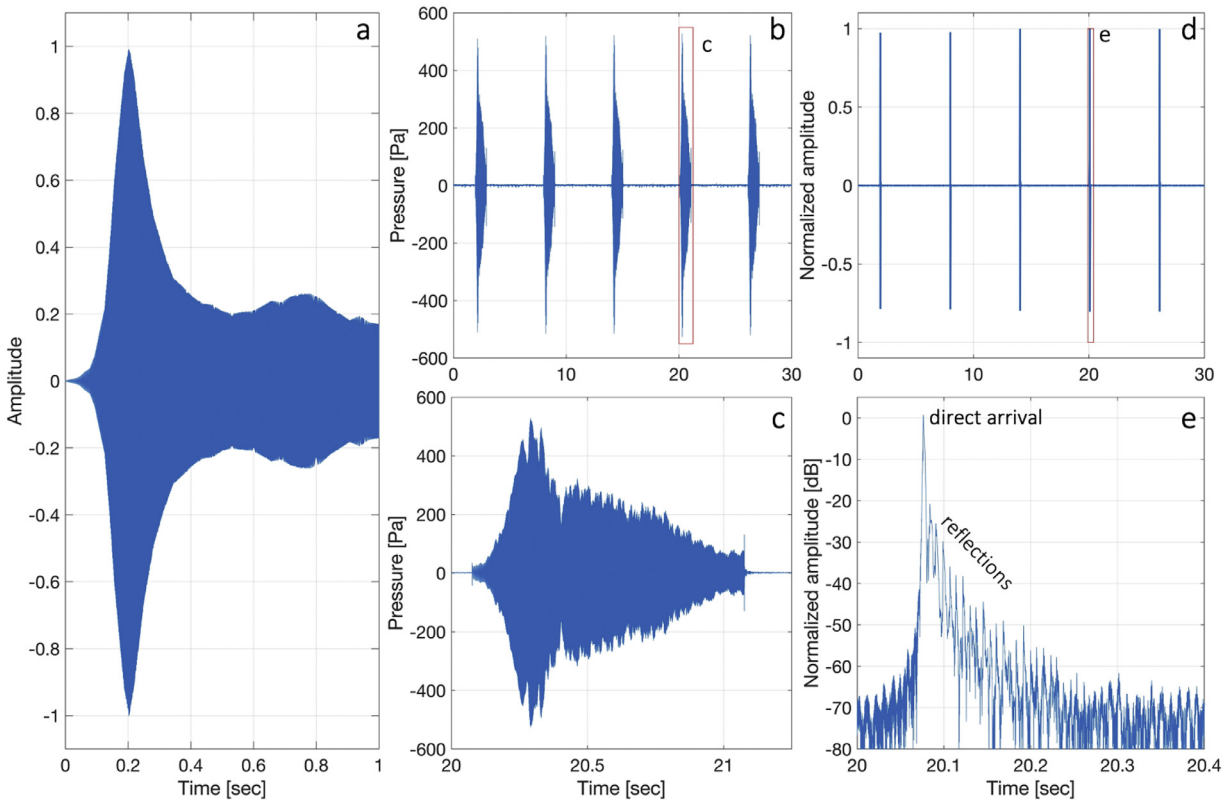


**Fig. 5.** Example of the recorded acoustic data: a) radiated acoustic signal corrected to frequency response of the sound source, b) recorded raw sound pressure and c) its zoomed part, d) recorded signal after cross-correlation with the radiated one and e) its zoomed part.

(red curve). For this specific dataset, $c_{best}$ = 197m/s, 95% confidence interval of the estimated sound speed is $c_{0.95}$ = 178 – 216m/s, $\Theta_{gas_{best}}$= 0.23%, and $\Theta_{gas_{0.95}}$ = 0.19 – 0.29% (Fig. 2b).

*Step-by-step operation procedure*

*Acoustic experiment and data acquisition*

In this section, we presuppose that the reader has all the equipment delineated in Section 1.3 and is proficient in the use of MATLAB for all the computational purposes. Prior to engauging with the Analog Discovery 3 (AD3), it is imperative to install the Waveforms software — a dedicated application for AD3 and the requisite Digilent and Instrument Control MATLAB toolbox. Then, establish a connection between the sound source and the hydrophone to the output and input terminals of AD3, respectively. Position both the sound source and the hydrophone at an identical depth, separated by 1 meter, refer to Fig. 1 for visual clarification. For the computation of the optimal depth of your acoustic system, refer to [22]. It is critical to ensure that the deployment depth does not surpass the maximum threshold for the sound source, which is 12 m for the LUBELL-9162 model. Emit a sequency of 50 to 100 chirps, each with a duration of 1 second and a frequency range from 300 to 2000 Hz and record the acoustic data with the hydrophone. Frequency band of your signal may be different if you use another sound source. Frequencies must be chosen so that the source is omnidirectional over the entire frequency range. Utilize the chirp function in MATLAB to generate the signal. Refer to MATLAB's Instrument Control Toolbox manual to find necessary functions to connect to AD3 and enable unput and output terminals.

*Processing of acoustic data*

Perform a cross-correlation between the raw experimental data and the emitted chirp signals to extract the impulse response function, utilizing the xcorr function. Extract the impulse response envelope with the hilbert function and take its absolute value. Segment the resulting data into 1-second intervals and organize these segments into a matrix denoted as $\boldsymbol{B}_{exp}(\boldsymbol{n},\boldsymbol{t})$, where $\boldsymbol{n}$ corresponds to the impulse number and $\boldsymbol{t}$ to time. Then, compute the normalized impulse response functions in decibels (dB) using the following equation:

$$\boldsymbol{B}^{\boldsymbol{dB}}(\boldsymbol{n},\boldsymbol{t}) = 20\log_{10}\frac{\boldsymbol{B}_{\boldsymbol{exp}}(\boldsymbol{n},\boldsymbol{t})}{\max\left(\boldsymbol{B}_{\boldsymbol{exp}}(\boldsymbol{n},\boldsymbol{t}\right)} \tag{6}$$

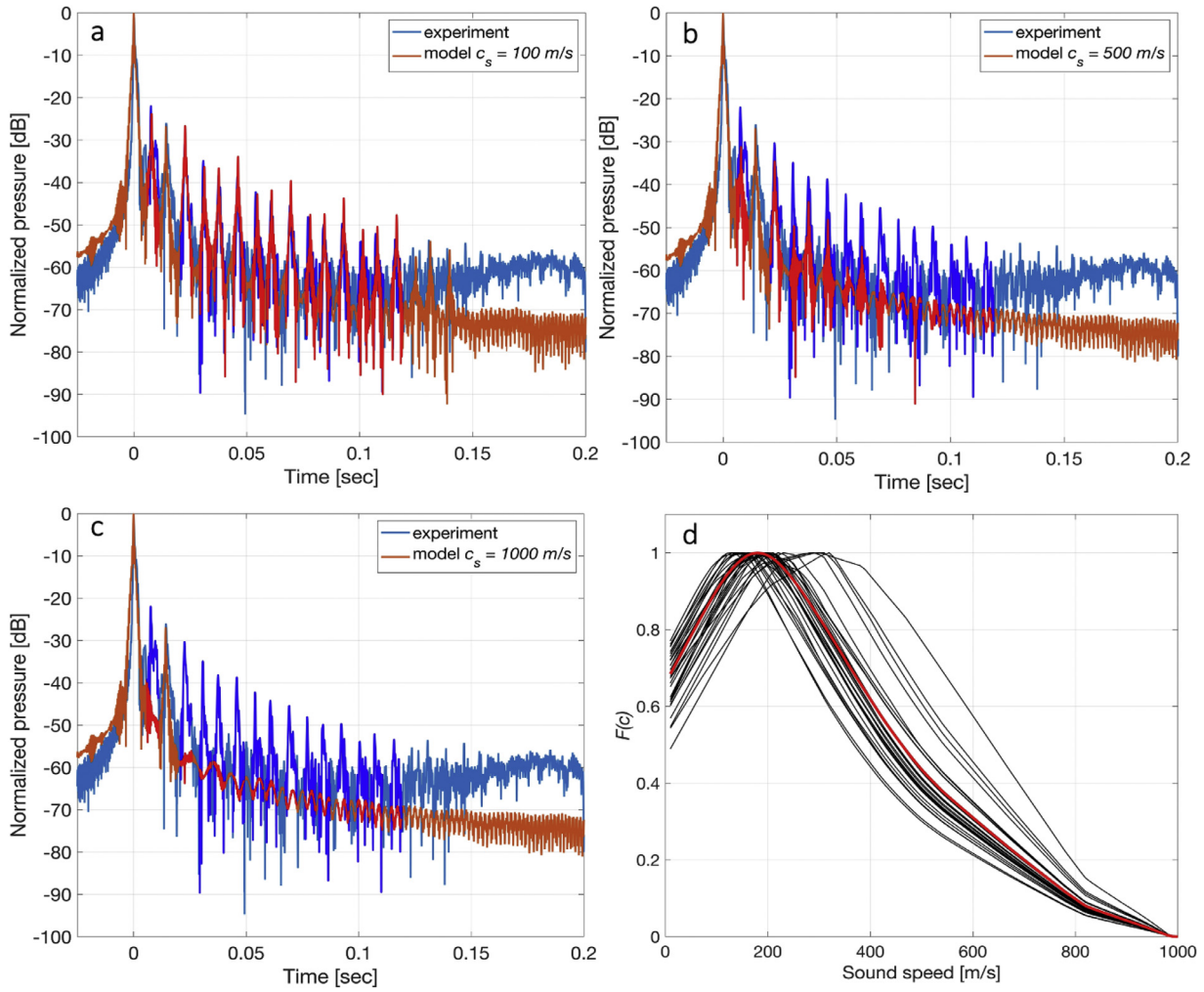


**Fig. 6.** Matching the experimental (blue) and modeled (red) pulse signals for different sound speeds, $c$, in the sediment of Lake Kinneret, Israel, during the experiment conducted in May 2019. Reflections used for comparison between the experiment and simulations are highlighted in bright red and blue colors, respectively. The simulated pulses were calculated by Eq. (3) for the following sound speeds, $c$: a) 100 m/s, b) 500 m/s, c) 1000 m/s. d) The normalized cost function $\boldsymbol{F(c)}$ (Eq. (5)) was calculated via matching each radiated pulse to simulation performed for sound speeds ranging from 10 m/s to 1500 m/s with increment of 10 m/s.

In the model of the sound field, as per Section 1.2, the sound speed in the sediment, denoted as $c$, is the sole variable parameter. Maintain all other parameters (Table 2) as constants. You may have to adjust those parameters to match your water reservoir (lake, river, etc.) properties. It makes sense to take several sediment cores prior modeling to assess its composition and porosity. Within the sound speed range, for example, 100 – 1600 m/s, calculate the sound field using Eq. (3). Normalize the calculation by 1 and convert into the dB scale (as detailed in Eq. (6)) to derive $\boldsymbol{B^{dB}_{mod}(t,c)}$. These modelled sound fields are then compared to the experimental impulse response function $\boldsymbol{B^{dB}_{exp}(n,t)}$ using Eq. (5). Peak position, $t_i$, of each arrival in $\boldsymbol{B^{dB}_{mod}(t,c)}$ can be identified by the findpeaks function. For an illustrative example, refer to Fig. 6d, where black curves denote individual pulses, and the red curve signifies the average of all functions $\overline{\boldsymbol{F(c)}} = \frac{1}{N}\sum_{n=1}^{N} \boldsymbol{F_n(c)}$. Estimate margin of error as in Section 1.4. Finally, associate the determined sound speed values with the corresponding gas fractions as per Eq. (1).

## Regression analysis and methane production empirical modeling

The multiannual (2015–2021) sediment gas content estimations in Lake Kinneret, Israel, are performed by the acoustic methodology described above in Section 1, and serve as a basis for the correlation analysis. A multivariate linear regression is fitted using the gas content as dependent variable Y, and predictors $X_n$ (or independent variables) that change temporally and spatially over the aquatic ecosystem and may serve as main controls on sediment gas content variability [24]. Significance of the predictor for the

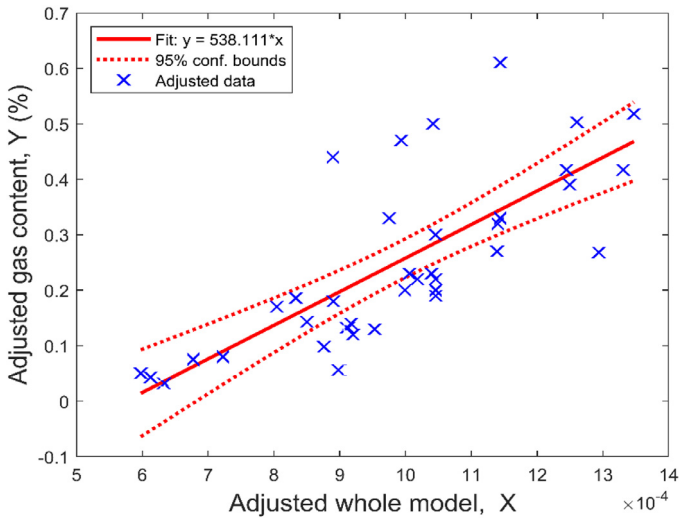


**Fig. 7.** Gas content, $\boldsymbol{Y}$ (%), correlation plot for whole-model-adjusted independent variable $\boldsymbol{X}$, along with 95% confidence boundaries (adopted from [25]).

correlation is defined by p-value (if p-value < 0.05, the predictor is significant for the correlation, otherwise it could be excluded from the correlation) [[24] and references therein]. The following predictors are suggested to control gas content, Y, in sediments of Lake Kinneret: $X_1$ – water depth, $X_2$ – $CH_4$ production rate, $X_3$ – $CH_4$ bubble dissolution rate, derived from the ecosystem analysis [25]:

$$\boldsymbol{Y} = \boldsymbol{A}_0 + \boldsymbol{A}_1 \times \boldsymbol{X}_1 + \boldsymbol{A}_2 \times \boldsymbol{X}_2 + \boldsymbol{A}_3 \times \boldsymbol{X}_3 + \boldsymbol{A}_4 \times \boldsymbol{X}_2 \times \boldsymbol{X}_3 \tag{7}$$

where $\boldsymbol{A}_0$ is an intercept and $\boldsymbol{A}_1$, $\boldsymbol{A}_2$, $\boldsymbol{A}_3$, $\boldsymbol{A}_4$ are the regression coefficients before the corresponding predictors. The interaction term between the geochemical factors ($\boldsymbol{X}_2 \times \boldsymbol{X}_3$) is also included in the correlation (Eq. (7)) and its significance is evaluated as well. Predictors may differ between the aquatic ecosystems [e.g., 26]. Every predictor may incorporate several specific effects (e.g., water depth predictor, $X_1$, used for the Lake Kinneret modeling [25], may be associated with variability of spatial $CH_4$ ebullition from sediment; with $CH_4$ bubble size dependence on mechanical muddy sediment properties that change over the lake; and with $CH_4$ solubility). The linear regression is used as the most general regression type [24], however, the non-linear regression may be tested if more accurate relations between Y and $X_n$ are known for other aquatic ecosystems.

Water depth (independent variable $X_1$) is evaluated at every acoustic measurement. $CH_4$ production rate in sediment (independent variable $X_2$) is evaluated using the empirical modeling suggested by Grasset et al. [27]. The temporal variability in the $CH_4$ production rate in sediment, $X_2$, is assumed to depend on the fresh, highly reactive organic matter deposition dynamics due to the phytoplankton crash (specific for the Lake Kinneret). The source of the organic matter and its deposition pattern may differ between the water bodies.

The model takes a fresh frequent Particulate Organic Matter (added POM) deposition to anoxic sediment as input. The model [27] is applicable for short time intervals (< 100 days), in contrast, for instance, to other models designed to simulate the $CH_4$ production over the entire sediment column applicable for longer time scales (e.g., [28]).

The time-dependent total $CH_4(t)$ production kinetics in sediment is presented as:

$$\boldsymbol{CH}_4(t) = \frac{\boldsymbol{Asym}}{1 + \boldsymbol{exp}\left[(\boldsymbol{xmid} - t)/\boldsymbol{scal}\right]}, \tag{8}$$

where t is time in days since the POM deposition and Asym is a reaction yield, defined as a horizontal asymptote at infinity, xmid corresponds to the t value at which $CH_4$ (t) reaches Asym/2, and scal is a distance between xmid and the point where $\boldsymbol{CH}_4(t) = \frac{\boldsymbol{Asym}}{1+e^{-1}}$.

For phytoplankton as an added POM to lake's bottom [27]:

$$\ln(\boldsymbol{Asym}) = -2.26 + 0.87 \times \ln(\boldsymbol{added\ POM}). \tag{9}$$

The total $CH_4$ production rates can thus be evaluated as [27]:

$$\boldsymbol{P}(\boldsymbol{CH}_4)(t) = \frac{\boldsymbol{CH}_4(t)}{\boldsymbol{scal}} \times \left(1 - \frac{\boldsymbol{CH}_4(t)}{\boldsymbol{Asym}}\right). \tag{10}$$

The maximum $CH_4$ production rate (the peak) in sediment preceding each acoustic measurement is defined as an independent variable $X_2$, which is used for our correlations.

The $CH_4$ gas dissolution rate (independent variable $X_3$, Eq. (7)) is suggested in our methodology to be inversely proportional to the time elapsed between the maximum $CH_4$ production peak and the acoustic measurement date, ΔT (in days, $X_3 = 1/\Delta T$). $X_3$ does not include any specific reaction kinetics. The longer the ΔT is, the greater the amount of $CH_4$ in bubbles in sediment that will dissolve

into the pore waters, assumed in our model. The interaction between the geochemical $CH_4$ production and gas bubble dissolution terms, $X_2$ and $X_3$, is introduced by their product term, $X_2 \times X_3$ (Eq. (7)).

The regression (Eq. (7)) is fitted using MATLAB (v.2023a) function fitlm (implemented in MATLAB internally using the QR decomposition method [29]). The multivariate regression is reduced to the univariate one for convenience of presentation and analysis, by introducing the adjusted whole model independent variable X. This is implemented in the fitlm function internally by using the Frisch–Waugh–Lovell theorem [30]. An example of gas content, $\boldsymbol{Y}$ (%), correlation plot for whole-model-adjusted independent variable $\boldsymbol{X}$, along with 95% confidence boundaries, is depicted in Fig. 7 (adopted from [25]).

## Ethics statements

Not applicable.

## Declaration of competing interest

The authors declare that they have no known competing financial interests or personal relationships that could have appeared to influence the work reported in this paper.

## CRediT authorship contribution statement

**E. Uzhansky:** Data curation, Formal analysis, Investigation, Methodology, Software, Validation, Visualization, Writing – original draft. **R. Katsman:** Conceptualization, Formal analysis, Investigation, Methodology, Resources, Visualization, Writing – original draft. **A. Lunkov:** Data curation, Investigation, Methodology, Validation, Writing – review & editing. **B. Katsnelson:** Data curation, Investigation, Methodology, Resources, Writing – review & editing.

## Data availability

Raw data used in the article can be found in the supplementary material

## Acknowledgments

This project was supported by the U.S.–Israel Binational Science Foundation (BSF), grant No. 2018150.

## Supplementary materials

Supplementary material associated with this article can be found, in the online version, at doi:10.1016/j.mex.2024.102799.

## References

[1] D.F. McGinnis, N. Bilsley, M. Schmidt, P. Fietzek, P. Bodmer, K. Premke, A. Lorke, S. Flury, Deconstructing methane emissions from a small northern european river: hydrodynamics and temperature as key drivers, Environ. Sci. Technol. 50 (2016) 11680.
[2] L. Liu, T. De Kock, J. Wilkinson, V. Cnudde, S. Xiao, C. Buchmann, D. Uteau, S. Peth, A. Lorke, Methane bubble growth and migration in aquatic sediments observed by X-Ray McT, Environ. Sci. Technol. 52 (2018) 2007.
[3] Y. Dück, L. Liu, A. Lorke, I. Ostrovsky, R. Katsman, C. Jokiel, A novel freeze corer for characterization of methane bubbles and assessment of coring disturbances, Limnol. Oceanogr. Methods 17 (2019) 305.
[4] E. Uzhansky, B. Katsnelson, A. Lunkov, I. Ostrovsky, Spatial and temporal variability of free gas content in shallow sediments: lake kinneret as a case study, Geo-Marine Lett. 40 (2020) 491.
[5] M.J. Buckingham, M.D. Richardson, On tone-burst measurements of sound speed and attenuation in sandy marine sediments, IEEE J. Oceanic Eng. 27 (2002) 429.
[6] J. Yang, D. Tang, K.L. Williams, Direct measurement of sediment sound speed in shallow water '06, J. Acoust. Soc. Am. 124 (2008) EL116.
[7] S.S. Fu, R.H. Wilkens, L.N. Frazer, Acoustic lance: new in situ seafloor velocity profiles, J. Acoust. Soc. Am. 99 (1996) 234.
[8] R.H. Wilkens, M.D. Richardson, The influence of gas bubbles on sediment acoustic properties: in situ, laboratory, and theoretical results from Eckernförde bay, Baltic Sea, Cont. Shelf. Res. 18 (1998) 1859.
[9] B.I. Goncharenko, I. Zakharov, V. Ivanov, V. Kirshov, Frequency and angular response of coefficient of sound reflection from a layered bottom, Soviet Phys. Acoustic 22 (1976) 197.
[10] Z. Tóth, V. Spiess, H. Keil, Frequency dependence in seismoacoustic imaging of shallow free gas due to gas bubble resonance, J. Geophys. Res. Solid. Earth. 120 (2015) 8056.
[11] I. Ostrovsky, J. Tegowski, Hydroacoustic analysis of spatial and temporal variability of bottom sediment characteristics in lake kinneret in relation to water level fluctuation, Geo-Marine Letters 30 (2010) 261.
[12] Z. Tóth, V. Spiess, J.M. Mogollón, J.B. Jensen, Estimating the free gas content in baltic sea sediments using compressional wave velocity from marine seismic data, J Geophys Res: Solid Earth 119 (2014) 8577.
[13] J. Li, P. Gerstoft, M. Siderius, J. Fan, Inversion of head waves in ocean acoustic ambient noise, J. Acoust. Soc. Am. 147 (2020) 1752.
[14] D.A. Bevans, M.J. Buckingham, Estimating the sound speed of a shallow-water marine sediment from the head wave excited by a low-flying helicopter, J. Acoust. Soc. Am. 142 (2017) 2273.
[15] E. Uzhansky, O. Gadol, G. Lang, B. Katsnelson, S. Copel, T. Kazaz, Y. Makovsky, Geoacoustic estimation of the seafloor sound speed profile in deep passive margin setting using standard multichannel seismic data, J. Mar. Sci. Eng. 9 (2021) 1.
[16] G. Mavko, T. Mukerji, J. Dvorkin, The Rock Physics Handbook (2009).
[17] L. Brekhovskikh Y. Lysanov, Fundamentals of Ocean Acoustics. (1991).
[18] F.V. Rozhin, O.S. Tonakanov, General Hydroacoustics, MGU, Moscow, 1988.

[19] B. Katsnelson, R. Katsman, A. Lunkov, I. Ostrovsky, Acoustical methodology for determination of gas content in aquatic sediments, with application to lake kinneret, israel, as a case study, Limnol. Oceanogr. Methods 15 (2017) 531.
[20] E. Uzhanskii, Estimation of gassy sediment parameters using remote acoustical methods: lake kinneret, north of israel as a case study, University of Haifa 147 (2018).
[21] B. Katsnelson, A. Lunkov, I. Ostrovsky, E. Uzhansky, Estimation of gassy sediment parameters from measurements of angular and frequency dependencies of reflection coefficient, Proc. Meetings Acoustics 33 (2019) 1.
[22] B.G. Katsnelson, E. Uzhansky, A.A. Lunkov, I. Ostrovsky, Characterization of gassy layer of sediment in shallow water using acoustical method. lake kinneret as a case study, Limnol. Oceanogr. Methods 20 (2022).
[23] R. Katsman, A. Lunkov, E. Uzhansky, B. Katsnelson, Effective model of gassy sediments and acoustical approach for its verification, 6th Underwater Acoustics Conf. Exhibition 44 (2021) 005001.
[24] G.A.F. Seber A.J. Lee, Linear Regression Analysis, (2003).
[25] R. Katsman, E. Uzhansky, A. Lunkov, B. Katsnelson, Methane gas dynamics in sediments of lake Kinneret, Israel, and their controls: insights from a multiannual acoustic investigation and correlation analysis, Sci. Total Environ. 918 (2024) 170480.
[26] L. Marcon, K. Sotiri, T. Bleninger, A. Lorke, M. Männich, S. Hilgert, Acoustic mapping of gas stored in sediments of shallow aquatic systems linked to methane production and ebullition patterns, Front. Environ. Sci. 10 (2022) 1.
[27] C. Grasset, S. Moras, A. Isidorova, R.M. Couture, A. Linkhorst, S. Sobek, An empirical model to predict methane production in inland water sediment from particular organic matter supply and reactivity, Limnol. Oceanogr. 66 (2021) 3643.
[28] A. Isidorova, C. Grasset, R. Mendonça, S. Sobek, Methane formation in tropical reservoirs predicted from sediment age and nitrogen, Sci. Rep. 9 (2019) 1.
[29] R.E. Welsch, Robust regression using iteratively reweighted least-squares, Commun. Stat. Theory. Methods 6 (1977) 813.
[30] M.C. Lovell, Seasonal adjustment of economic time series and multiple regression analysis, J. Am. Stat. Assoc. 58 (1963) 993.